Microarrays of Vertically-Aligned Carbon Nanofiber Electrodes in an Open Fluidic Channel

Timothy E. McKnight,*,†,‡,§ Anatoli V. Melechko,†,|| Derek W. Austin,†,|| Tyler Sims,†,⊥ Michael A. Guillorn,†,‡,§,⊥ and Michael L. Simpson†,‡,§,⊥

Oak Ridge National Laboratory, Oak Ridge, Tennessee 37831, and University of Tennessee, Knoxville, Tennessee 37996

Received: December 23, 2003; In Final Form: March 12, 2004

Fabrication and electrochemical characterization of microarrays of individually addressable vertically aligned carbon nanofiber electrodes contained within an open fluidic channel are described. Compatibility of the deterministic synthesis of vertically aligned nanofibers with conventional microfabrication techniques enables the development of relatively complex, functional multilevel devices that may be produced efficiently in large numbers. The vertical orientation of nanofibers provides a basis for small volume electroanalyses in probing regions elevated above the planar substrate, which can enable applications including electroanalysis within and around live cell matrixes, high aspect ratio probing structures for scanning electrochemical microscopy, and channel-resident electrodes with high capture efficiency for electrochemical detection of microfluidic chemical separations.

Introduction

Nonplanar ultramicroelectrodes have become important tools in the study of chemical and electrochemical dynamics and for small volume electroanalyses.[1] Microcylindrical or semihemispherical electrodes at the ends of sheathed probing structures have provided the basis for scanning electrochemical microscopy with high spatial resolution[2] and are often the method of choice for electrochemical detection of microfluidic separations.[3] Their application has also provided significant insight into dynamic physiological processes, enabling the observation of fast time-constant events in and around living cells such as the exocytotic release of neurotransmitters.[4]

Conventionally, nonplanar micro- and nanoscale electrodes are fabricated using techniques that require production on an individual basis. For example, in electrophysiological applications, single electrodes are often fabricated by encapsulating a microscale electrode material (for example, fine wire or a carbon filament) within a glass capillary tube and thermally pulling this assembly down to microscale dimensions. Upon cleaving in the vicinity of the electrode material, the glass tube provides a sheath of electrical insulator and only a small area at the tip of the device is electrochemically active. Another common technique is to chemically or electrochemically etch an electrode material down to a fine point, followed by application of a sheathing material to the sidewalls of the electrodes by, for example, electrodeposition or physical coating techniques.[5−7] Here the amount of exposed electrochemically active tip can be controlled by careful application technique, such as by having the desired tip remain above the surface of the electrodeposition solution or by exploiting material property changes of the sheathing, such as thermally induced shrinking of a polymeric coating in order to expose the nanoscale tip.

Wafer-scale microfabrication methods used for semiconductor processing have enabled higher throughput production of microelectrode systems.[8] Often, these methods are used to generate *disk*, *band*, and *ring* electrodes which exploit the massive parallelism possible with microfabrication but provide only planar electrode structures, which are not well suited for applications where access to analyte volumes *above* the planar substrate are required. Top-down fabrication methods employing anisotropic etching techniques, such as reactive ion etching and focused ion beam milling, can provide nonplanar, high aspect ratio structures that extend above the planar substrate, but there are often material and feature size limitations associated with the former and the latter has a disadvantage of being a serial process where each individual feature must be separately milled. Recently, bottom-up approaches have emerged in which desired nanostructures are produced in a massively parallel, self-assembly process. Among such methods are catalytic chemical vapor deposition of carbon nanostructures (nanotubes and nanofibers).[9−13]

Controlled synthesis of vertically aligned carbon nanofibers by catalytic plasma enhanced chemical vapor deposition (C-PECVD) provides new opportunities for mass production of electrochemical devices that feature high-aspect ratio vertical structures well-suited for electrochemical analyses. Catalytically synthesized nanofibers may be deterministically grown in a vertical orientation on a variety of substrates and feature nanoscale tip geometries and lengths of up to several tens of microns. The fiber growth process can be employed as an integral step in device microfabrication, thereby enabling the realization of complex multilevel devices that feature very high aspect ratio, nonplanar electrodes.[14,15] Previously, we[16] and others[17] have documented the fabrication of individually ad-

* Corresponding author: mcknightte@ornl.gov. Telephone: 1 865 574-5681. Fax: 1 865 574-1249.

† Molecular Scale Engineering and Nanoscale Technologies Research Group, Oak Ridge National Laboratory.

‡ Condensed Matter Sciences Division, Oak Ridge National Laboratory.

§ Engineering Science and Technology Division, Oak Ridge National Laboratory.

|| Department of Electrical and Computer Engineering, University of Tennessee.

⊥ Department of Materials Science and Engineering, University of Tennessee.

10.1021/jp037987m CCC: $27.50
Published on Web 05/01/2004

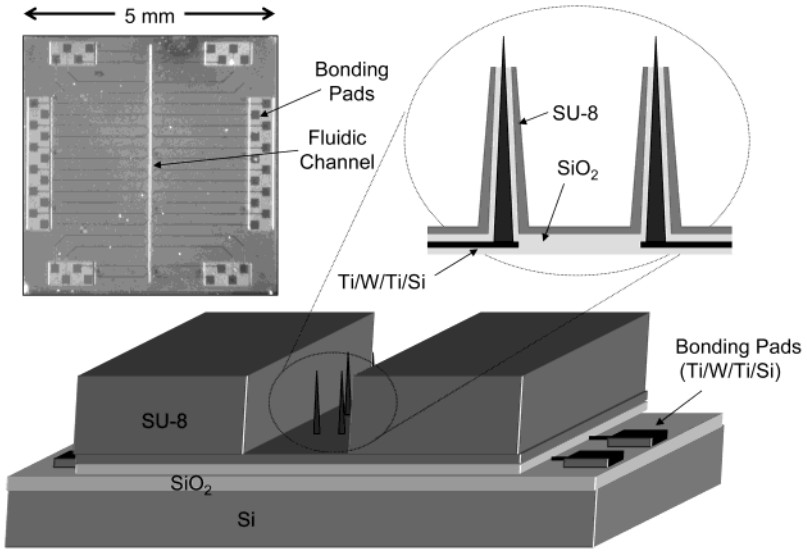

Figure 1. Schematic view of a nanofiber-based electrochemical probing array (not to scale) and photograph of a completed single die. Each chip features up to 40 individually addressable nanofiber probing elements (four shown in schematic view) within an open microfluidic channel with bonding pads located around the periphery of each die. Multiple layers of passivation localize electrochemical activity to the extreme tip of each nanofiber.

dressable nanofiber electrodes, and several groups have documented aspects of the electrochemical performance of regions of nanofiber forests[18,19] and sparse arrays of nanofibers.[20] Ultimately, such devices may be employed to interrogate and manipulate biological matrixes, such as living cells and tissue, where the nanofiber serves as a vertical element on a planar substrate that can penetrate within the biological matrix, including the intracellular domain of cells.[21] The parallelism of microfabrication, however, enables this integration to be achieved on a massively parallel basis with many cells interfaced to nanofibers across a large array of nanofiber electrodes.

In this work, vertically aligned carbon nanofibers are implemented as individually addressable electrochemical probes at size scales designed to enable the integration of these structures into viable cells and tissue matrixes (submicrometer radii, and typically sub 100 nm radii and micron lengths). We explore the integration of these features into devices using wafer-scale microfabrication processes and characterize the electrochemical performance of these systems.

Device Fabrication

Deterministic Synthesis of Carbon Nanofibers. Our methods for nanofiber synthesis have been extensively described in the literature[11−13] and will not be discussed here in detail. In brief, VACNFs are synthesized in a dc-plasma enhanced chemical vapor deposition process (dc-PECVD) where a carbonaceous source gas (e.g., acetylene) is decomposed upon the top surface of nickel catalyst particles and deposited in a highly ordered manner beneath the catalyst. The location(s) of fiber growth on a substrate are defined by lithographic patterning of thin nickel films. In the first stage of the growth process, these Ni films coalesce to form nanoparticles, each of which catalytically generates a single nanofiber. In our dc-PECVD process, the nanofiber substrate serves as the cathode of the dc-plasma and nanofibers grow oriented along the electric field lines, vertically aligned perpendicular to the substrate.[11] The radial dimensions of the nanofibers are determined by the size of the catalyst particle, although plasma parameters can also influence fiber radius and morphology (cylindrical or conical).[12] Fiber length is controlled by the growth time, which for PECVD is determined by the time the plasma is on. As nanofiber location, size, shape, and orientation can be controlled, we refer to our fiber growth process as "highly deterministic". The high level of determinism allows the nanofibers to be crafted to fit the needs of specific applications, such as in this case the generation of vast arrays of nanofibers well-suited for high resolution, small volume electrochemical probing.

Design Layout of Integrated Probing Device. The format of the embodiment of a VACNF probe array characterized in this work is shown in Figure 1. This multilevel device features up to 40 individually contacted vertically aligned carbon nanofiber probes clustered together in groups of four, all within a microfluidic channel (a single group of four probes is illustrated in Figure 1). Multiple layers of electrical insulation, including a conformal coating of silicon dioxide and multiple layers of a UV curable epoxy, SU-8 (Microchem), are used to confine electrochemical activity at the nanofiber elements and to provide mechanical protection of the fibers within the microfluidic channel. These devices are fabricated using wafer-scale processing, with a 4" silicon wafer yielding approximately 100 completed devices (all layers of passivation) and 100 additional partially processed devices that can be used for quality control evaluations (for instance, regions of the wafer lack several passivation layers in order to provide inspection of parts following full wafer processing).

Overview of the Device Fabrication Process. Our individually addressable nanofiber array fabrication approach was previously reported[16] and is briefly described here. Details of important new aspects of the fabrication process are emphasized following this overview. The overall fabrication process is outlined in Figure 2. Alignment marks for subsequent projection and contact photolithography steps are patterned onto 4" diameter silicon wafers with 1 μm thick thermal oxide using a GCA Autostep 200 5X reduction stepper. These patterns are then etched into the oxide layer using a CHF_3/O_2 based reactive ion etch (RIE) (Trion Oracle). The wafers are then coated with 100 Å of Ti, 1000 Å of W, 100 Å of Ti, and 100 Å of Si using electron-gun physical vapor deposition at 10^{-6} Torr (Figure 2A). In the next photolithography procedure, the sites for fiber growth are defined in SPR 955CM-0.7 resist (Shipley) as 500 nm diameter circular patterns (Figure 2B) and 400 Å of nickel is deposited using electron-gun physical vapor deposition followed

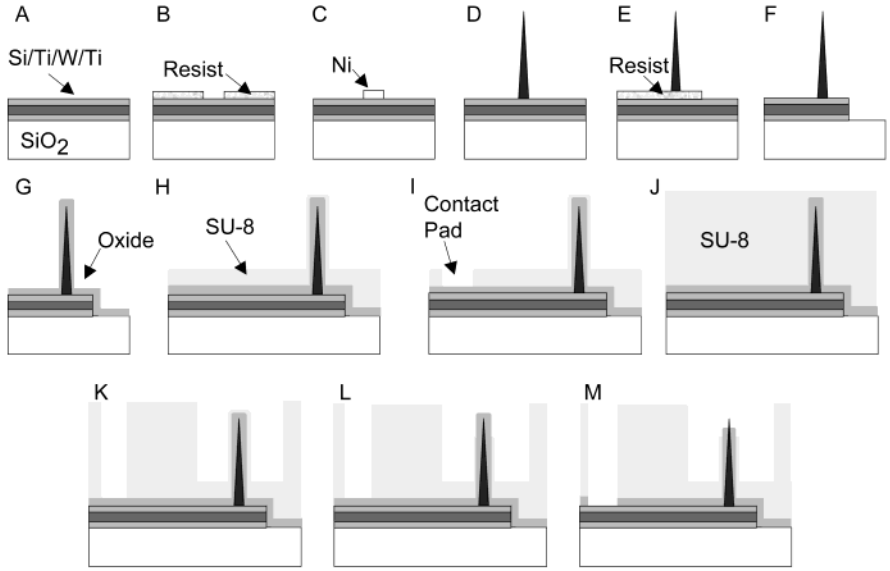

Figure 2. Fabrication of individually addressable nanofiber electrochemical probes within a microfluidic channel. Individual steps are described in the text.

by lift-off (Figure 2C). Fiber synthesis is conducted in a dc-plasma enhanced chemical vapor deposition process (dc-PECVD) where catalytic decomposition of acetylene on nickel results in tip-type nanofibers and the catalyst particle is elevated off the substrate and remains at the fiber tip during and after growth (Figure 2D). During this growth, the underlying metallization (Ti/W/Ti/Si) serves as the cathode for the dc-plasma. Following fiber growth, electrode interconnects are patterned with photoresist that is used as an etch mask during RIE removal of the metal outside interconnects (Figure 2E). First, a CF_4-based silicon etch removes the surface layer of Si, followed by a $SF_6/CF_4/O_2$-based refractory metal etch to remove the underlying Ti, W, and Ti (Figure 2F). A passivation layer of ~100 nm of PECVD silicon dioxide is coated conformally on all surfaces (interconnects, substrate, and fibers; Figure 2G), and a subsequent passivation layer of 2 μm of SU-8 is spun onto the wafer (Figure 2H). Contact pads are lithographically defined in the SU-8 photoresist layer (Figure 2I). A second layer of SU-8 resist is then spun on at a thickness greater than the length of the nanofibers, typically 15−20 μm (Figure 2J). Fibered regions and contact pads are cleared of this SU-8 layer using contact photolithography (Figure 2K). An oxygen-based SU-8 dry etch process is then used to remove (ash) residual SU-8 resist and to emancipate the oxide-coated nanofiber tips from any SU-8 residual that has accumulated on the fiber surface (Figure 2L). Finally, a CHF_3/O_2-based silicon dioxide reactive ion etch process is used to emancipate the nanofiber tips from the silicon dioxide and to open the peripheral contact pads (Figure 2M).

Catalyst Preparation Using Photolithography. The entire sequence is performed using only *photolithography*, thus enabling rapid and efficient wafer-scale synthesis. This is an alternative method to our previous reported approaches to individually addressable nanofiber device fabrication, where electron-beam lithography was used to define sites of fiber growth.[16] The sites of fiber growth upon a substrate are determined by the patterning of nickel catalyst thin films, as in Figure 2C. During initial phases of fiber synthesis, the nickel film breaks up and coalesces into particles, each of which catalyzes the growth of a single nanofiber. Particle nucleation of nickel thin films is dependent upon a number of factors, including the thickness, size, and geometry of the thin film (i.e., its aspect ratio), the quality of the film, interaction between the nickel and the underlying substrate, and plasma conditions during particle nucleation. To realize *singular* nanofibers upon an interconnect, the size of the initial catalyst dot must be defined such that the film coalesces into *only* one particle during the initial phases of fiber growth. In previous efforts, this has been accomplished predominantly by minimizing the geometric size of nickel catalyst thin films. For example, to nucleate singular particles from nickel thin films on a Ti/W-coated substrate, the geometric size of a 100 Å nickel film was limited to a diameter of <100 nm. This was achieved using electron-beam lithography and a lift-off process. While effective, electron-beam lithography is a serial writing process and, therefore, can pose as a rate or resource limiting step in microfabrication. As such, we sought alternative approaches to defining nickel films that would nucleate singular particles for nanofiber synthesis.

In this effort, we have employed an approach[22] that enables single particle nucleation from nickel thin films up to at least 600 nm in diameter. The patterning at these feature sizes can easily be accomplished with reduction stepper photolithography, deep UV lithography, and perhaps even with contact lithography, thus eliminating the requirement for serial writing using electron-beam lithography. In this approach, a silicon layer is deposited prior to nickel deposition. In the pregrowth steps of nanofiber synthesis, this silicon layer facilitates nucleation of singular nickel particles from larger geometry films due to the interfacial characteristics of these two materials. Additionally, to provide a proper aspect ratio of the larger films, thicker nickel films are used with optical lithography than are used with electron-beam lithography. In the current work, nickel films of 400 Å on a thin (100 Å) silicon layer successfully nucleated individual particles from film regions of 400−700 nm in diameter. Nanofibers with tip radii down to approximately 30 nm have been generated using this photolithographic process, in part due to the presence of the Si interfacial layer that facilitates formation of a single Ni particle from the lithographically defined Ni film. The devices of this work feature fibers with tip radii from approximately 50 nm to 200 nm.

While the silicon layer facilitates singular particle formation, it can also potentially impart significant resistance at the nanofiber/interconnect interface. In this work, the Si layer was

100 Å thick and the resistance of this layer did not appear to significantly impact electrode performance. This may be due, in part, to Ni-metal induced crystallization of the silicon layer which forms polycrystalline silicon of increased conductivity at elevated temperatures and therefore may result during PECVD nanofiber synthesis.[23]

Insulating and Structural Function of Epoxy-Based Photoresist. Interconnect and probe insulation is an important aspect of any electrochemical probing system. Conventionally, fabrication of nanoscale electrodes involves reducing the tip diameter of microscale electrode materials using a variety of etching techniques followed by processing to insulate all but the nanoscale tip of the device.[5] The axial format of these traditional nanoscale electrodes enables controlled immersion of the electrode tip into an analyte and only requires quality passivation of the immersed section of the portions of the device that need to be insulated. Nonetheless, the quality of insulation is important as defects, such as pinholes and cracks, will contribute to the measured redox response of the electrode if they enable electron transfer between the underlying electrode and the analyte solution. Also, even defect-free insulation layers can contribute significantly to the measured electrode response via capacitive coupling with the analyte solution. This contribution is often the limiting factor in fast-scan voltammetric techniques as the capacitance current (noise) scales with the scan rate of the experiment.[24] As such, with these traditional single element nanoscale probes, multiple thick layers of insulating materials are typically used to reduce the capacitive response of the probe.

The electrochemically active surface area of a nanofiber-based probe will be dependent upon a number of factors including the amount of nanofiber that is exposed from the oxide and SU-8 sheath, surface contaminants upon this exposed tip, and pinholes and other defects at various points along the passivated interconnect. Ultimately, it is desirable that only the extreme tip of each fiber is electrochemically active, to have high spatial resolution in probing applications. This is complicated by the planar format of the interconnect structure in nanofiber array substrates where long (i.e., mm) interconnects run between the active nanoscale probe and bonding pads located at the periphery of the device. Compared to the nanoscale dimensions of the desired active probing regions, these long interconnects are large, potentially-"immersed" surface areas that could contribute significant noise during electroanalyses, either via undesired redox activity at defect sites or due to capacitive coupling. In previously reported embodiments, a single layer of PECVD silicon dioxide was used as insulating coating of the fibers and interconnects of individually addressable nanofiber arrays. In this work, three layers of passivation are employed, including a thin ($<$150 nm) coating of PECVD oxide upon the fibers and interconnects, a 2$-$3 μm thick layer of spun-on SU-8 photoresist on the interconnects, and a second 15$+$ μm thick layer of SU-8 photoresist. The last layer of SU-8 is also used to define a fluidic channel in which the nanofibers are positioned. The thin layer (50$-$150 nm) of PECVD silicon dioxide is deposited on the entire device. The sole purpose of this layer is to provide *sheath insulation* of each nanofiber element. In this capacity, it is desirable to have this layer as thin as possible such that the increased sheath diameter of the insulated probes does not limit their application for penetration and probing of living cells. However, as the thickness of this layer is decreased, there is an increased probability of defect sites in the form of pinholes and cracks in the oxide as well as an increased capacitive contribution of this dielectric layer to the measured response of the probe. Thus, the amount of thickness of the oxide requires optimization between minimizing the ultimate diameter of the insulated probes while still providing a level of passivation adequate to reduce the noise contribution of defects and capacitance of this dielectric layer. It is for this reason that the PECVD oxide layer is used solely for insulating the sheath of nanofibers. The longer stretches of interconnects on the substrate are passivated with an additional layer of SU-8, a UV cross-linked epoxy also referred to as a negative tone photoresist. A relatively low viscosity formulation of SU-8 (SU-8 2002) is spun onto the wafer at 1800 rpm, which results in approximately 2.5 microns of SU-8 on the substrate of the device. As an epoxy-based photoresist, this material is relatively electrochemically inert and can be patterned photolithographically to provide for access to underlying structures, i.e., the metal bonding pads at the periphery of each device. By spinning this material on the substrate, a relatively thick layer of SU-8 passivates the underlying interconnects while the high aspect ratio nanofibers emerge above the spun-on layer. However, this approach does not completely eliminate "thickening" of the nanofibers. As a negative-tone photoresist, the SU-8 is cross-linked in exposed regions (the bulk of each device) and developed away in unexposed regions (bonding pads). To cross-link the SU-8 and thereby passivate the underlying interconnects at the base of nanofibers, the nanofiber region of the device must be exposed. However, some SU-8 will coat and remain on the nanofibers even after the spin process. Upon exposure, this SU-8 will cross-link on the fibers, and will contribute to their overall diameter. As with the silicon dioxide layer, it is desired to minimize this thickening of fibers as much as possible both to satisfy cellular penetration requirements and to avoid contamination of the probe with materials that might impact electrochemical performance.

Packaging of the Devices. Following spin, exposure, and development of the first layer of SU-8, a second layer of thick SU-8 is spun onto the wafer of devices. This final layer provides additional passivation of the underlying interconnect but is employed primarily as a mechanical protection layer and as a structural element to facilitate packaging and use of the electrode array. This final layer is spun on at a thickness greater than the length of the fibers and then is lithographically patterned to (again) expose the peripheral bonding pads and to define a microfluidic channel in which the fiber arrays are located. In this layout, fibers are mechanically protected by being recessed within the microfluidic cavity of the final SU-8 layer. This is particularly useful during packaging of the die into functional devices. Following microfabrication, individual die (5 mm square) are diced from the wafer and mounted in 40-pin ceramic dual in-line package (DIP) carriers. The chips are wirebonded to provide electrical interconnects between the DIP package and the die. Having the nanofiber electrodes recessed within a fluidic cavity enables them to be protected during the potting of these wire interconnects. The microfluidic channel on the die is temporarily capped with a small rectangular block of solid poly(dimethylsiloxane) (PDMS) to protect the recessed nanofiber electrodes, and the entire device is backfilled with a nonconductive epoxy in order to passivate the bonding pad regions and wirebonding material from participating as electrochemically active sites. Following epoxy cure, the temporary PDMS cap is removed and the device is ready for use as electrochemical probes or for subsequent chemical modification and/or cellular interfacing.

Fiber Passivation Removal and Electrochemical Activation. In Figure 2 steps L and M, carbon nanofiber electrodes are emancipated from passivation in order to generate an electro-

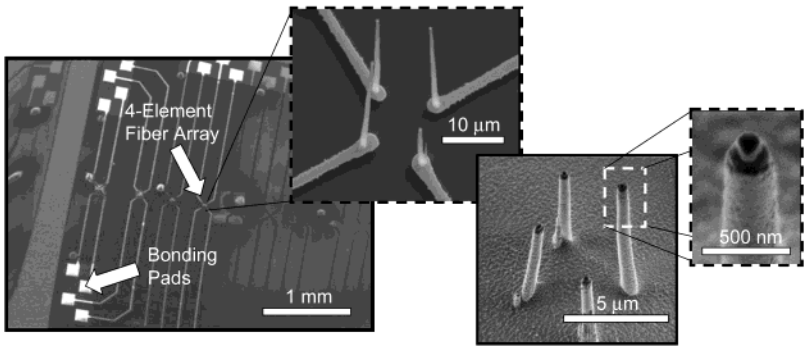

Figure 3. Scanning electron micrographs of an individual chip of 40 nanofiber probing elements. At far left, image taken following the oxide deposition step and prior to SU-8 passivation (Figure 2G) to facilitate imaging the underlying interconnect structure (first inset). At right, a four-element array is shown following device completion. Individual fibers feature oxide and some SU-8 passivation, with only the extreme tip being exposed for electrochemical activity. SU-8 on the substrate hides the underlying interconnect structure in these images.

chemically active surface area at the tip of each probing element. In this effort, we employ an anisotropic dry etch process to expose only the extreme tip of each probe. First, an oxygen plasma etch is used to remove residual SU-8 that may have coated the fibers during the first SU-8 spin and which becomes cross-linked during SU-8 exposure. Following removal of SU-8, a subsequent oxide reactive ion etch is used to remove the PECVD oxide and thus expose the underlying electrochemically active surface area of the carbon fiber. This emancipation process can be used at a wafer scale at several steps during the fabrication process. For example, it may be performed after the first SU-8 layer has been spun and exposed or after the second layer of SU-8 has been spun and the channels are defined with SU-8 development. In earlier work, tip emancipation has been performed after the PECVD oxide deposition step by first spinning the substrate in a protective layer of positive tone photoresist (Shipley 1818) such that the underlying interconnect passivation is protected from the oxide etch process. We have also buried the nanofibers in deeper layers of photoresist (SPR220) to enable longer oxide etch processes to remove oxide from essentially all regions of the nanofibers which emerge above the resist layer (data not shown). In addition to these wafer-scale approaches to nanofiber tip emancipation, chips diced from the wafer may also be individually processed, thus enabling some variability in the amount of tip exposed on an individual chip basis.

As a point of comparison, we have also evaluated wet etching of the oxide layer using 6:1 buffered HF. This wet etch has been quantified to etch our PECVD oxide films at a rate of approximately 150 nm/min. A 90 s HF etch can be used to remove the PECVD oxide (50−150 nm thick) at exposed fiber regions without stripping significant amounts of the SU-8 covered interfacial oxide that protects underlying metal interconnects upon the substrate. Wet etching does not appear to require a preceding oxygen plasma etching to remove spun-on and cross-linked SU-8 on the fibers. Rather, this material tends to be shed from the fibers when the underlying layer of oxide is etched by the buffered HF. It must be noted, however, that, in contrast to RIE, wet etching is relatively isotropic and, therefore, removes all exposed oxide and not just oxide at the tips of fibers. Implementation of a buffered HF process for tip emancipation would therefore require alteration of the fabrication scheme to include (prior to the final SU-8 layer passivation) a fiber burial in photoresist (1800 series or SPR220), tip emancipation from resist with oxygen plasma, and wet etching of these exposed tips in buffered HF, followed by removal of the protective photoresist layer with acetone prior to incorporating the final layer of SU8.

Results and Discussion

Device Inspection with Microscopy. Devices at various stages of completion are shown in Figure 3. At 10 points along the microfluidic channel, groups of four addressable nanofiber electrodes are positioned at various interfiber gaps (2, 4, 6, 8, and 10 μm). All surfaces except the bonding pads at the periphery and the tips of each fiber are passivated, such that electrochemical activity is limited to the extreme tip of each nanofiber. Passivation includes ~100 nm of silicon dioxide and 2.5 μm of SU-8 over the entire device (except bonding pads) and another 15+ μm of SU-8 covering the device except for in the fluidic channel regions in which the nanofiber electrodes are located and at the bonding pads. Scanning electron microscopic surface imaging of a completed dielectric-covered structure can be achieved without surface modification (without metallic sputtered coatings) at acceleration voltages from approximately 1−2 kV. Partially passivated structures (oxide and first SU-8 layer) can be imaged at higher accelerating voltages (10 kV) to reveal underlying interconnect features, although charging will occur at these accelerating voltages. Also, SU-8 is optically transparent at the thicknesses used in these devices, thus facilitating the use of optical microscopy for interconnect and alignment inspections.

Characterization of Electrical Interconnect Insulation by Electrodeposition of Metals. Electrodeposition of gold may be used to reveal defect sites in these passivation layers, provided significant overpotential is applied to overcome a resistive drop in what could be nanoscale pinholes and cracks in the passivation. We evaluated the passivation quality of partially completed devices (prior to the final spinning of thick SU-8 Figure 3I) by emancipating fiber tips and pads from oxide and SU8, electrically connecting to individual bonding pads, and performing gold depositions with a commercially available plating solution (Orotherm HT Gold) at very high overpotentials (−1 V beyond set-on of gold deposition). Electron microscopy was used to inspect for gold deposition and thus defect sites in the passivation. Electrochemical activity was observed to be limited almost entirely to the nanofibers on the device, with only a few very small defect sites in the passivation of the underlying metal interconnect structure. We anticipate these defects are passivated further under the final SU-8 layer of completed devices. Also, in early samples, gold nucleation was observed emerging from the base of nanofibers, apparently due to incomplete exposure of the SU-8 layer beneath the fibers during this lithographic step (Figure 2I). The fibers are not always perfectly normal to the surface and therefore can shadow the SU-8 at underlying regions at the base of the fiber during

exposure. This results in incomplete exposure of the shadowed SU-8 and removal of this passivation at the fiber base during SU-8 development. Overexposure of the SU-8 during this lithographic step (3X the manufacturer's recommended dose) appears to have eliminated this problem.

Electrical and Electrochemical Characterization of Nanofiber Electrodes. Individually addressable nanofiber electrode response was evaluated using several quasi-reversible, outer sphere redox species, including ruthenium hexamine trichloride, potassium hexachloroiridate, and potassium ferrocyanide. Electroanalyses were performed with a commercially available three-wire potentiostat (CH Instruments model 660A electrochemical analyzer). In all evaluations, the reference electrode was Ag|AgCl in 3 M KCl which was contained within a 2-mm diameter glass tube and separated from the analyte volume by a porous glass frit. Due to the micro- and nanoscale active working electrode areas, analysis currents were typically <10 nA and therefore required only a two-wire configuration (working and reference electrode) without use of a counter electrode. The reference electrode was immersed directly into analysis volumes above the 5 mm chip array and positioned approximately 1 mm above the surface of the device. Connections to individual nanofiber elements (working electrodes) were made by connecting leads to individual pins of the ceramic dual-in line package carrier in which each array chip was mounted. Interconnect resistances were determined by fabricating array chips that featured nanofiber interconnects that were *not* isolated in the nanofiber region during the interconnect lithography step (Figure 2E and F). These devices featured groups of four leads that were commonly connected in the center of the device and therefore provided the ability to measure lead resistance from one bonding pad to other bonding pads of the interconnected leads. Interconnect resistance was determined to be <1 kΩ to the fiber in all devices tested ($n = 5$ chips, 5 interconnect sets each), which matched closely to expected values based on the interconnect metallization geometry, thickness, and resistivity.

The capacitance of individually addressable nanofiber elements (and interconnects) was determined by observing capacitive current at various scan rates in 100 mM KCl and performing linear regression analysis of the relation $I = C\,\mathrm{d}V/\mathrm{d}t$, where I is the capacitive charge current, C is the capacitance, and $\mathrm{d}V/\mathrm{d}t$ is the sweep rate of the voltammetric scan. The values obtained with these measurements include the summation of capacitive contributions of the electronics, macroscopic electrical connections to the device package (40 pin DIP), planar interconnect structure, and the solution interface capacitance of the nanofiber electrode. The contribution of this latter factor was estimated by performing linear regression analysis of total electrode capacitance of completely emancipated fibers (oxide sheath removed with buffered HF treatment) with different lengths and therefore varying geometric surface area (Figure 4). Geometric surface area of individual fiber electrodes was estimated by dimensional measurements of each fiber from scanning electron micrographs. The resulting surface area dependence of the total capacitance was estimated to be ~140 μF/cm^2 of exposed nanofiber, which is slightly higher than published values for carbon-based electrodes (2−120 μF/cm^2).[25] The higher value may be due to surface roughness of the fibers and, thus, larger actual (microscopic) surface areas than those estimated by geometry. Higher capacitance may also result due to surface oxides.

The total capacitance of RIE-emancipated nanofibers, where only the extreme tip of the electrode is intentionally cleared of dielectric, and their interconnects was determined to be 40 ± 5 pF ($n = 5$), which corresponds well with the data presented in Figure 4 assuming an exposed nanofiber surface area of <2 μm^2. To validate this surface area, dimensional measurement provided only a rough estimate of the exposed tip surface area. Therefore, a more accurate approximation was determined with cyclic voltammetry of a quasi-reversible outer sphere redox species, 10 mM $Ru(NH_3)_6Cl_3$. Individual electrodes were considered to be semihemispherical microelectrodes, where the extreme tip of the nanofiber protrudes from the oxide layer of the sheath in a semihemispherical geometry. The electroactive surface area of these probes could thus be approximated by measuring the steady-state reduction current of $Ru(NH_3)_6^{+3}$ and calculating the radius of the electrode using the steady-state current relationship vs microelectrode radius

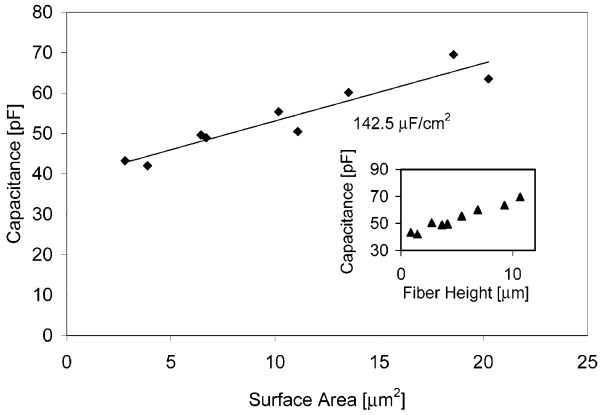

Figure 4. The capacitance of individually addressed nanofiber probes of varying height (inset) and geometric surface area. The linear dependence of capacitance upon surface area (as indicated by solid line) corresponds to a solution/electrode interface capacitance of 142.5 μF/cm^2, which is slightly higher than reported values for carbon electrode capacitance.

$$r = \frac{i_{ss}}{2\pi nFDC} \tag{1}$$

where i_{ss} is the measured steady-state reduction current, $n = 1$ (for a one-electron-transfer reaction), F is Faraday's constant, D is the diffusion coefficient of $Ru(NH_3)_6^{+3}$ in 100 mM KCl, and C is the concentration (10 mM). For all probes tested, the calculated radius was <250 nm, thus providing an active surface area of $<4 \times 10^{-9}$ cm^2.

The voltammetric potential windows of an individual carbon fiber electrode in various air saturated aqueous supporting solutions are provided in Figure 5. Carbon electrodes are often cited as featuring wide potential windows in aqueous media, where "potential window" refers to the potential range over which the electrode can be used without significant electrolysis of the supporting solution. For carbon electrodes in aqueous solutions, hydrolysis of water is typically the potential window-limiting reaction, observed in these voltammograms as significant increases in current at the cathodic (hydrogen evolution) and anodic (oxygen and/or chlorine evolution) termini. Additionally, saturation of solutions with air results in cathodic peak(s) associated with oxygen reduction which can be significant sources of noise for measurements requiring sensitivity at concentrations below approximately 1 mM, due to the presence of oxygen in the solution (expected oxygen concentration in solution at 1 atm pressure of dry air is 8.6 mg/L[26]).

The responses of tip-exposed individual nanofiber electrodes to ruthenium hexamine trichloride, potassium hexachloroiridate, and potassium ferrocyanide are provided in Figure 6. Voltam-

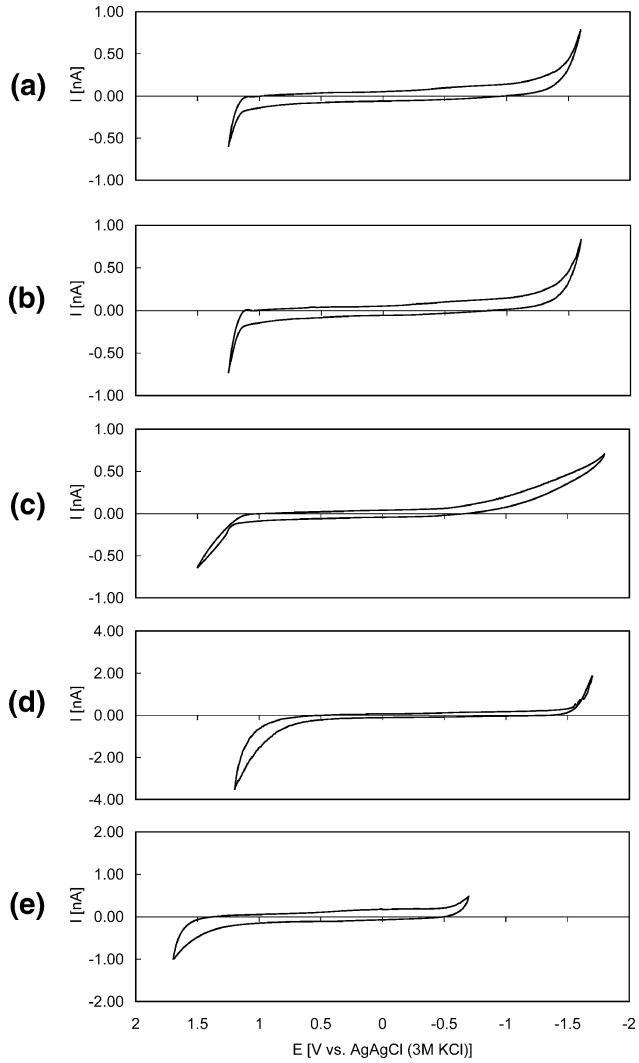

Figure 5. Voltammetric potential window of an RIE emancipated individually addressable nanofiber, in (a) 100 mM KCl, (b) phosphate buffered saline, (c) methanol, (d) 1 N sodium hydroxide, and (e) 1 N sulfuric acid. All solutions are air saturated. Scan rate is 200 mV/s.

metry was performed in 1 and 10 mM solutions of these species in 100 mM KCl at scan rates of 200 mV/s. As indicated, individual electrodes provide steady-state voltammetric currents for these quasi-reversible outer sphere species due to the radial diffusion of analyte to and away from the active electrode surface. However, comparison of measured steady-state currents against those expected from assumed semihemispherical electrodes of known radii (as measured by scanning electron microscopy) indicates that the steady-state currents are significantly reduced from expected values. We anticipated that the presence of nickel catalyst particles on the emancipated tips of nanofibers might interfere with redox activity in these regions and effectively diminish the overall electrochemically active area. Nickel metal in neutral aqueous environments quickly forms an oxide layer (NiO) which provides little electrochemical activity and therefore would essentially present a passivated surface at these exposed regions of the fiber.[27] Therefore, to observe if the presence of nickel catalyst at the tips of fibers was diminishing overall electrode response, chemical treatment was conducted to remove the nickel particles from nanofibers and voltammetry was repeated. Wetted portions of an array chip were chemically etched in 65% nitric acid for a period of 60 s, followed by an extensive rinse in deionized water. This treatment has been established to remove nickel catalyst particles from

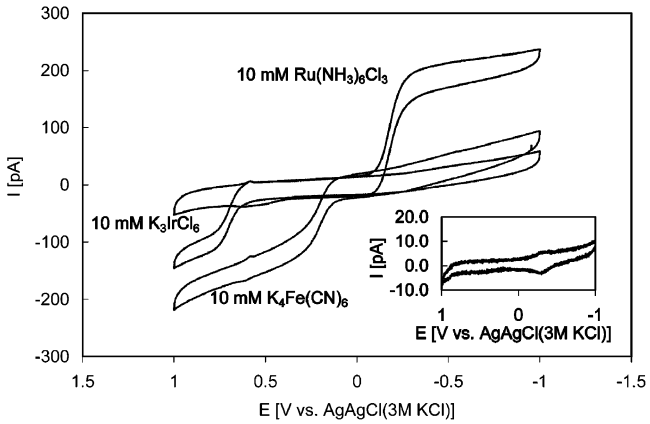

Figure 6. Response of tip exposed nanofiber electrodes to 10 mM solutions of potassium hexachloroiridate, potassium ferrocyanide, and ruthenium hexamine trichloride in 100 mM KCl (scan rate 200 mV/s). Inset: the response of oxide sheathed (unreleased tip) nanofiber electrodes following exposure to 1 mM ruthenium hexamine trichloride. The observed peaks appear to correspond to a surface confined species on the fibers.

nanofiber tips provided the nickel is exposed to the acid solution and not capped by a carbon passivation layer which is often found on the tips of nanofibers after synthesis.[28] Subsequent voltammetry of nickel catalyst-free nanofibers provided significant increases in steady-state response, with values approaching expected values based upon semihemispherical electrode geometries of known radii, as estimated with electron microscopy.

Evaluation of Silicon Dioxide Layer as an Insulating Sheath. To evaluate the quality of the oxide passivation layer upon nanofiber electrodes, several array chips were fabricated without emancipating the carbon fibers from the passivating oxide sheath and these chips were evaluated with voltammetry. During the oxide removal steps of the fabrication process (Figure 2 steps L and M), the microfluidic channel regions of these chips were capped with a solid poly(dimethylsiloxane) block. Capping the channel protected the fibers from the reactive ion etch but enabled the removal of oxide from the peripheral bonding pads, allowing wirebonding and interconnection to the packaged chips, but not release of the fiber tips. Cyclic voltammetry was performed in 1 mM ruthenium hexamine trichloride in 100 mM KCl, resulting in the response indicated in Figure 6 inset. As evidenced by the absence of redox waves corresponding to the $Ru(NH_3)_6^{+2/+3}$ couple, the oxide sheathing appears to be of adequate quality. However, the oxidation and reduction of a surface bound species is clearly distinguished in this background subtracted voltammogram, as evidenced by a pair of redox waves with a peak separation close to zero. These peaks occur at a potential (−0.32 V) which corresponds with surface waves previously observed following both ruthenium hexamine trichloride exposure and oxygen plasma etching of larger scale nanofiber forest electrodes.[18] This may result from the presence of surface bound oxides upon the fibers.

Evaluation of Fully Released Fiber Electrodes. In addition to evaluating tip emancipated and unemancipated nanofiber electrodes, fibers that were *completely* released from passivation by dissolving the PECVD oxide with buffered HF were also investigated. The responses of HF released electrodes of various lengths exposed to 10 mM ruthenium hexamine trichloride are provided in Figure 7. Again, steady-state voltammetric responses are predominantly indicated, with currents proportional to the overall exposed length (and therefore surface area) of the nanofiber electrode. It is interesting to note that deviation from

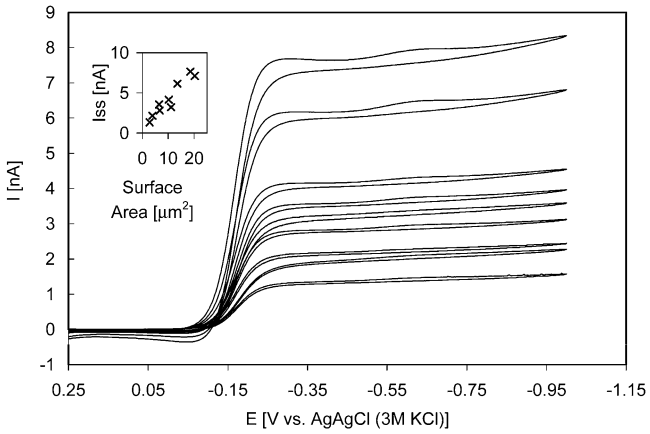

Figure 7. Cyclic voltammogram of independent nanofiber probes of varying length following complete oxide emancipation using HF dip. Analyte: 10 mM $Ru(NH_3)_6^{+3/+2}$ in air saturated 100 mM KCl at a scan rate of 200 mV/sec. Inset: steady-state current dependence upon the geometric surface area of individual fibers as estimated by dimensional measurement with scanning electron microscopy.

the steady-state response is observed as electrode height and surface area increases, as indicated by diffusion-limited peaking at low overpotentials of the oxidation and reduction wave. It is well established[29] that cylindrical ultramicroelectrodes do not feature steady-state current limits but rather manifest a quasi-steady-state response at long time limits where

$$i_{qss} = \frac{2nFADC}{r \ln \tau} \text{ where } \tau = \frac{4Dt}{r^2} \qquad (2)$$

and t is the time scale of the experiment and all other factors are the same as those in eq 1. The electroactive surface of short nanofiber electrodes and nanofibers with sheath passivation (active tips) can be described as semihemispherical and subscribe more to the steady-state response of that geometry. However, as exposed fiber length increases, the response moves from that of a semihemispherical microelectrode to that of a cylindrical microelectrode, and a quasi-steady-state response is seen. Further, in the geometric confines of the microfluidic channel, this quasi-steady-state condition may be exaggerated due to additional restrictions upon the diffusion of analyte to the surface; i.e., at the experimental scan rates, $Ru(NH_3)_6^{+3}$ is reduced slightly faster than can be supplied via diffusion. Further, the reduced species can accumulate slightly within the channel region around the electrode to be oxidized during the reverse scan, thus resulting in the indicated peaking of the response at the cathodic and anodic termini of the redox wave.

The current density dependence upon geometric surface area of these nanofiber microcylinder electrodes is provided in Figure 8 for 1 mM and 10 mM ruthenium hexamine trichloride in 100 mM KCl. As before, geometric surface area was determined by approximation from dimensional measurements of scanning electron micrographs of each fiber electrode. For comparison, for each concentration of analyte, the response of an ideal semihemispherical microelectrode of identical surface area is also plotted (solid line). For these calculations, the radius of a semihemisphere of equivalent geometric surface area was used to determine the steady-state reduction current using the relationship of eq 1. The resultant steady-state current was then divided by the hemispherical surface area to obtain the theoretical current density. The result is a fair approximation of the response of our microcylindrical electrodes, even for the longer fiber electrodes.

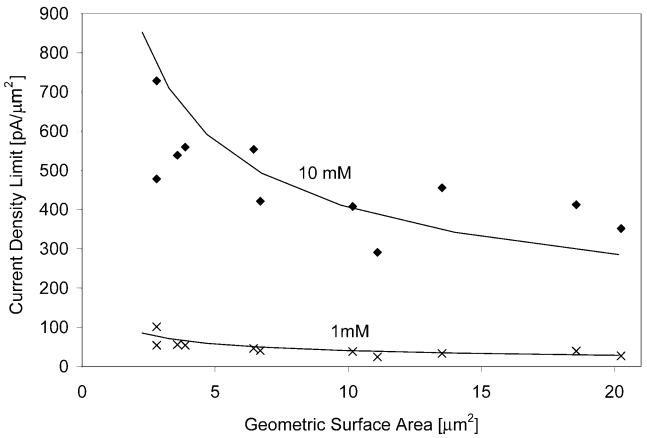

Figure 8. Steady-state current density of various length (and therefore surface area) nanofiber probes. The solid lines are calculated expected current densities from electrodes with semihemispherical geometry of indicated total surface areas.

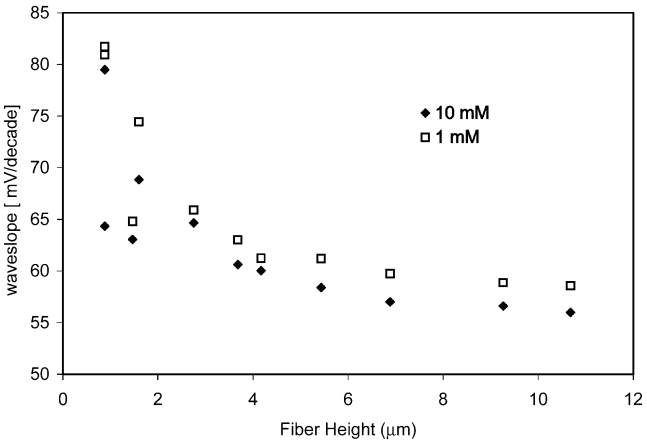

Figure 9. Waveslope dependence on electrode height for ruthenium hexamine trichloride reduction on HF emancipated nanofiber electrodes.

Ruthenium hexamine trichloride is widely established as a quasi-reversible outer sphere redox species for carbon electrode systems. As such, the slope of the oxidation and reduction waves should closely approach the analytical ideal which is expected to be

$$\frac{2.303RT}{nF} = \frac{59.1}{n} \text{ mV} \qquad (3)$$

at 25 °C, where R is the molar gas constant, 8.314 47 J/mol K, T is the temperature, and F is Faraday's constant, 96 485.3 C/mol. At laboratory conditions of 20 °C, this waveslope value decreases to 58.3 mV/n. Figure 9 presents the waveslope of buffered HF emancipated nanofibers (completely unsheathed from oxide) of various geometric surface areas at 1 and 10 mM concentrations of ruthenium hexamine trichloride in 100 mM KCl. The waveslope was calculated by performing linear regression analysis of the applied potential (E) vs $\log[(i_{lim} - i)/i]$ for the portion of the wave in the region from approximately $E_{1/4}$ and $E_{3/4}$ (the potentials of the redox wave where the current has changed by $^1/_4$ and $^3/_4$ of the steady-state current). With a few outlying data points, the dataset appears to converge to a value of approximately 59 mV/decade for 1mM and approximately 56 mV/decade for the 10 mM analyte concentration. In the former case, near ideal behavior is observed for the larger surface area electrodes, but for both cases, smaller electrodes deviate significantly from this behavior. Also, for the 10 mM analyte, the longer electrodes converge upon a waveslope that

is less than the expected analytical value. It is possible that this response is due to enhanced mass transport to the electrode surface due to migration of the polycationic $Ru(NH_3)_6^{+3}$ to the negatively biased electrode. In 100mM KCl, the support ratio (γ: the ratio of the concentration of the supporting electrolyte to the concentration of the reactant) is only 10, and therefore there may be insufficient supporting electrolyte to obviate migrational effects of the analyte in the solution to the negatively biased electrode. It is well established that insufficient supporting electrolyte can dramatically impact the steady-state current at ultramicroelectrodes due to migrational enhancement of the reactants. This phenomena is dependent upon several factors, including the support ratio, electrode radius (and thus double layer and depletion layer overlap), and the charges upon the reactant species and their products as well as the charges upon the counterions of the supporting electrolyte.[30] The $Ru(NH_3)_6^{+3/+2}$ system has been studied for ultramicroelectrodes with radii down to approximately 1 μm with and without KCl as supporting electrolyte.[31] In this study, without supporting electrolyte, ($E_{3/4} - E_{1/4}$) increased vs the same value in excess supporting electrolyte as electrode radius decreased. The limiting current, i_{lim}, also increased vs the same value in excess supporting electrolyte, but this increase diminished as electrode radius decreased. As such, it is difficult to determine if insufficient electrolyte is the root cause for this observed phenomenon on the waveslope of our nanofiber probes. Further insight could be garnered through modeling of these mechanisms and indeed several successful analytical models have been developed,[32,33] but this is beyond the scope of this present article.

Characterization of Independence of Individual Probes in an Array. The electrical/electrochemical independence of neighboring nanofiber elements in 8-μm and 10-μm-spaced electrode arrays was evaluated using both gold electrodeposition and chronoamperometry experiments. For the former, gold electrodeposition onto individual nanofiber electrodes was conducted using a commercially available gold plating solution, as outlined in earlier sections. Gold deposition was observed via electron microscopy to be restricted to individually addressed nanofiber electrodes, with no obvious plating, and therefore "cross talk" to adjacent probes. Chronoamperometry experiments were conducted in 10 mM ruthenium hexamine trichloride using probe arrays that had been emancipated from oxide using the buffered HF process, thereby removing all silicon dioxide on the fiber sheath (and thus maximizing the measurable responses of these electrodes). The amperometric response of a *collector* nanofiber element clamped at the oxidizing potential of 0 V vs AgAgCl (3 M KCl) was observed during step application and removal of the reducing potential of -0.5 V vs the same reference electrode on an adjacent *generator* electrode (Figure 10a). At the oxidizing potential 0 V, the collector electrode indicated negligible amperometric response, as the bulk analyte solution was comprised of the already oxidized species, $Ru(NH_3)_6^{+3}$. Upon application of the reducing potential of -0.5 V at the adjacent generator electrode, $Ru(NH_3)_6^{+2}$ was produced and diffused to a steady-state concentration profile around the generator electrode. The reduced species could then be reoxidized on the collector, and this oxidation current measured. Figure 10b presents the oxidizing current detected on the collector electrode in response to $Ru(NH_3)_6^{+2}$ produced via step changes in 10 mM $Ru(NH_3)_6^{+3}$ reduction at a generator nanofiber electrode at a distance of 10 μm from the collector. Per eq 1, the steady-state current at a microelectrode is directly proportional to the concentration of analyte in the bulk. Thus, the measured response at the monitored electrode can be compared to the measured response of a known concentration of $Ru(NH_3)_6^{+2}$ to find the concentration of this species at the collector during these experiments. At steady state, the concentration of $Ru(NH_3)_6^{+2}$ arriving at the collector electrode, due to production at the 10 μm distant generator electrode, is approximately 0.8 ± 0.15 mM.

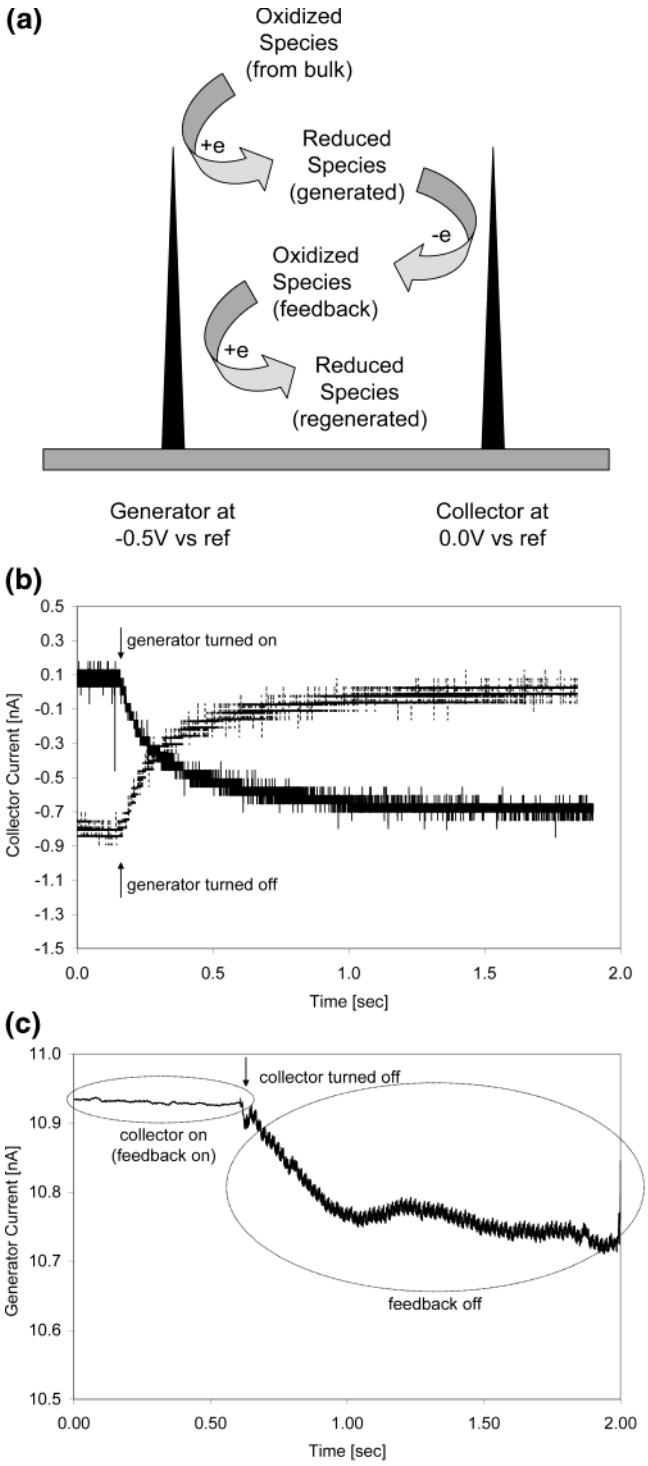

Figure 10. (a) Schematic of generator collector operation of a microfabricated nanofiber electrode couple for 10 mM ruthenium hexamine trichloride. (b) Amperometric response of the collector electrode upon activation and deactivation of the generator electrode 10 μm distant. (c) Demonstration of generator-collector feedback between two microcylinder nanofiber electrodes spaced 10 μm apart. Here, the amperometric response of the generator is shown for the scenario where feedback is on (collector active) and abruptly turned off (collector current stopped).

Generator-Collector Feedback Mechanism in Proximity Electrode Systems. In addition, we evaluated the *generator-collector feedback mechanism*, as described by Bard[29] between this electrode pair. In this phenomena, the close proximity of ultramicroelectrodes enables a feedback mechanism which can enhance the flux of electroactive species to the generator electrode, above that available from the bulk solution. For example, in a bulk solution of oxidized analyte, the *generator* electrode reduces oxidized species and provides a flux of the reduced species to an adjacent *collector* electrode (as described above and shown in Figure 10b). At the collector, this reduced analyte is reoxidized. Some of this reoxidized species can, in turn, return to the generator to again be reduced. Ultimately, this adds to the flux of oxidized species from the bulk solution to the generator and therefore provides an enhanced amperometric signal at this electrode. In Figure 10c, the amperometric response of the *generator* nanofiber microcylinder electrode in 10 mM ruthenium hexamine trichloride is shown. The generator electrode is clamped at the reducing potential of −0.5 V vs Ag|AgCl, while an adjacent collector electrode at 10 μm distance is connected (0 V vs Ag|AgCl) and disconnected (open circuit) from the reference electrode. When connected, the reduced species ($Ru(NH_3)_6^{+2}$) produced at the generator electrode and arriving at the collector is reoxidized. In turn, some of this reoxidized analyte returns to the generator and can again participate in the reduction reaction at the generator, resulting in feedback enhancement of the reduction current. When disconnected, the reduced species simply diffuses from the system without becoming reoxidized, and no feedback is observed. In the scenario of our 10 μm spaced microcylinder nanofiber electrodes, this feedback results in approximately a 2% increase in the steady-state reduction current at the generator electrode, where 0.8 mM $Ru(NH_3)_6^{+2}$ arrives at and is oxidized by the collector electrode and approximately 0.2 mM of this reoxidized $Ru(NH_3)_6^{+3}$ diffuses back to the generator.

Summary

We have presented the fabrication and characterization of microfabricated devices that feature multiple microarrays of electrochemically active vertical probing electrodes located within the confines an open fluidic channel. The devices documented in this work exploit the synthesis of carbon nanofibers, which provide the ability to grow nonplanar, high aspect ratio, electrochemically active structures at desired locations upon a device and which are very compatible with many microfabrication techniques. These devices may be fabricated in a massively parallel fashion, using wafer-scale processing techniques including lithography, thin film metal deposition, PECVD dielectric deposition, and wet and dry etching. Using these conventional microfabrication processes, nanofiber arrays can be generated such that only the extreme nanoscale tips of the vertical fibers are electrochemically active, or the devices can be processed such that entire fibers are totally released from passivating oxide. Microfabrication also enables the generation of microarray devices where the active elements are physically located within recessed cavities and/or microfluidic channels. In this study, the microfluidic channel aspects of the device were not emphasized beyond the fact that they provide structural elements to facilitate device packaging (such as potting following wirebonding) as well as mechanical protection of the nanofiber elements during use. However, the fabrication process is easily modified to provide for fluidic manifolds that might be more conducive to specific applications. For instance, for microfluidic-based chemical separation and analysis, the extension of vertical nanofiber elements into a closed channel may prove to offer superior capture efficiency over conventional planar electrodes that are integrated into the sidewalls of microfluidic separation platforms. Further, having only an active tip on these electrodes enables location of the sensing element in the center of the fluidic channel, which might provide higher resolution for the detection of eluted bands by isolating the measurement point from band broadening effects that occur at the sidewalls of the channel.

Using ruthenium hexamine trichloride as a diagnostic electrochemical species, we have established the electrochemical performance of as-fabricated nanofiber electrodes. We have examined the ability to individually address these high aspect ratio structures and have characterized their electrochemical response including their electrochemical potential window, capacitance, steady-state current responses during voltammetry, and the interelectrode communication phenomena often referred to as "generator/collector feedback". As this mechanism is useful for diagnosis and quantification of chemical reactions involving the oxidized and reduced species, this demonstration of microfabricated generator-collectors *in vertical configurations (above the planar substrate)* at well controlled spatial distances provides basis for advanced application of these techniques in scanning electrochemical microscopy, microfluidic channel electrochemical detection, and ultimately cell probing applications.

Acknowledgment. The authors wish to thank P. H. Fleming for assistance with metal depositions and D. Hensley for fiber synthesis. This work was supported in part by the National Institute for Biomedical Imaging and Bioengineering under assignment 1-R01EB000433-01 and through the Laboratory Directed Research and Development funding program of the Oak Ridge National Laboratory, which is managed for the U.S. Department of Energy by UT-Battelle, LLC.

References and Notes

(1) Wightman, R. M.; Wipf, D. O. Voltammetry at ultramicroelectrodes. *Electroanal. Chem.* **1989**, *15*, 267.

(2) Bard, A. J.; Fan, F. F.; Kwak, J.; Lev, O. Scanning electrochemical microscopy; introduction and principles. *Anal. Chem.* **1989**, *61*, 132.

(3) Wallingford, R. A.; Ewing, A. G. Capillary zone electrophoresis with electrochemical detection. *Anal. Chem.* **1987**, *59*, 1762.

(4) Wightman, R. W.; Jankowski, J. A.; Kennedy, R. T.; Kawagoe, K. T.; Schroeder, T. J.; Leszczyszyn, D. J.; Near, J. A.; Diliberto, E. J.; Viveros, O. H. Temporally resolved catecholamine spikes correspond to single vesicle release from individual chromaffin cells. *Proc. Natl. Acad. Sci. U.S.A.* **1991**, *88*, 10754.

(5) Chen, S.; Kucernak, A. Fabrication of carbon microelectrodes with an effective radius of 1 nm. *Electrochem. Commun.* **2002**, *4*, 80.

(6) Strein, T. G.; Ewing, A. G. Characterization of submicron-sized carbon electrodes insulated with a phenol-allylphenol copolymer. *Anal. Chem.* **1992**, *64*, 1368.

(7) Shulte, A.; Chow, R. H. A simple method for insulating carbon fiber microelectrodes using anodic electrophoretic deposition of paint. *Anal. Chem.* **1996**, *68*, 3054.

(8) Klemic, K. G.; Klemic, J. F.; Reed, M. A.; Sigworth, F. J. Micromolded PDMS planar electrode allows patch clamp electrical recordings from cells. *Biosens. Bioelectron.* **2002**, *17* (6−7), 597.

(9) Ren, Z. F.; Huang, Z. P.; Xu, J. W.;. Wang, J. H.; Bush, P.; Siegal, M. P.; Provencio, P. N. Synthesis of large arrays of well-aligned carbon nanotubes on glass. *Science* **1998**, *282* (5391), 1105.

(10) Meyyappan, M.; Delzeit, L.; Cassell, A.; Hash, D. Carbon nanotube growth by PECVD: a review. *Plasma Sources Sci. Technol.* **2003**, *12*(2), 205.

(11) Merkulov, V. I.; Melechko, A. V.; Guillorn, M. A.; Simpson, M. L.; Lowndes, D. H. Alignment mechanism of carbon nanofibers by plasma-enhanced chemical vapor deposition. *Appl. Phys. Lett.* **2001**, *79*, 2970.

(12) Merkulov, V. I.; Guillorn, M. A.; Simpson, M. L.; Lowndes, D. H.; Voekl, E. Shaping carbon nanostructures by controlling the synthesis process. *Appl. Phys. Lett.* **2001**, *29*, 1178.

(13) Merkulov, V. I.; Hensley, D. K.; Melechko, A. V.; Guillorn, M. A.; Lowndes, D. H.; Simpson, M. L. Control mechanisms for the growth of vertically aligned carbon nanofibers. *J. Phys. Chem. B* **2002**, *106*, 10570.

(14) Guillorn, M. A.; Hale, M. D.; Merkulov, V. I.; Simpson, M. L.; Eres, G. Y.; Cui, H.; Puretzky, A. A.; Geohegen, D. B. Integrally gated carbon nanotube field emission cathodes produced by standard microfabrication techniques. *J. Vac. Sci. Technol., B.* **2003**, *21*, 957.

(15) Guillorn, M. A.; Melechko, A. V.; Merkulov, V. I.; Hensley, D. K.; Simpson, M. L.; Lowndes, D. H. Self-aligned gated field emission devices using single carbon nanofiber cathodes. *Appl. Phys. Lett.* **2002**, *81*, 3660.

(16) Guillorn, M. A.; McKnight, T. E.; Melechko, A. V.; Austin, D. W.; Merkulov, V. I.; Simpson, M. L.; Lowndes, D. H. Individually addressable vertically aligned carbon nanofiber-based electrochemical probes. *J. Appl. Phys.* **2002**, *91*, 3824.

(17) Moser, J.; Panepucci, R.; Huang, Z. P.; Li, W. Z.; Ren, Z. F.; Usheva, A.; Naughton, M. J. Individual free-standing carbon nanofibers addressable on the 50 nm scale. *J. Vac. Sci. Technol., B* **2003**, *21* (3), 1004.

(18) McKnight, T. E.; Melechko, A. V.; Guillorn, M. A.; Merkulov, V. I.; Doktycz, M. J.; Culbertson, C. T.; Jacobson, S. C.; Lowndes, D. H.; Simpson, M. L. Effects of microfabrication processing on the electrochemistry of carbon nanofiber electrodes. *J. Phys. Chem. B* **2003**, *107*, 10722.

(19) Li, J.; Cassell, A.; Delzeit, L.; Han, J.; Meyyappan, M. Novel three-dimensional electrodes: electrochemical properties of carbon nanotube ensembles. *J. Phys. Chem. B* **2002**, *106*, 9299.

(20) Tu, Y.; Lin, Yeuhe; Ren, Z. F. Nanoelectrode arrays based on low site density aligned carbon nanotubes. *Nano Lett.* **2003**, *3* (1), 107.

(21) McKnight, T. E.; Melechko, A. V.; Griffin, G. D.; Guillorn, M. A.; Merkulov, V. I.; Serna, F.; Hensley, D. K.; Doktycz, M. J.; Lowndes, D. H.; Simpson, M. L. Intracellular integration of synthetic nanostructures with viable cells for controlled biochemical manipulation. *Nanotechnology* **2003**, *14* (5), 551.

(22) Melechko, A. V.; McKnight, T. E.; Hensley, D. K.; Guillorn, M. A.; Merkulov, V. I.; Lowndes, D. H.; Simpson, M. L. Control of Catalyst Particle Formation for Large Scale Synthesis of Arrays of High Aspect Ratio Vertically Aligned Carbon Nanofibers. *Nanotechnology* **2003**, *14*, 1029.

(23) Choi, J. H.; Kim, D. Y.; Kim, S. S.; Park, S. J.; Jang, J. Polycrystalline silicon prepared by metal induced crystallization. *Thin Solid Films* **2003**, *440*, 1−4.

(24) Wipf, D. O.; Kristensen, E. W.; Deakin, M. R.; Wightman, R. M. Fast-scan cyclic voltammetry as a method to measure rapid heterogeneous electron-transfer kinetics. *Anal. Chem.* **1988**, *60*, 306.

(25) McCreery, R. L. Carbon Electrodes: Structural Effects on Electron-Transfer Kinetics. *Electroanalytical Chemistry*, Vol. 17; Bard, A. J., Ed.; Marcel Dekker: New York, 1991.

(26) Carano, M.; Holt, K. B.; Bard, A. J. Scanning electrochemical microscopy 49. Gas-phase scanning electrochemical microscopy measurements with a clark oxygen ultramicroelectrode. *Anal. Chem.* **2003**, *75*, 5071.

(27) Pourbaix, M. Atlas of electrochemical equilibria in aqueous solutions, National Association of Corrosion Engineers, Houston, TX, 1974.

(28) Melechko, A. V.; McKnight, T. E.; Guillorn, M. A.; Merkulov, V. I.; Ilic, B.; Doktycz, M. J.; Lowndes, D. H.; Simpson, M. L. Vertically aligned carbon nanofibers as sacrificial templates for nanofluidic structures. *Appl. Phys. Lett.* **2003**, *82* (6), 976.

(29) Bard, A. J.; Faulkner, L. R. *Electrochemical Methods: Fundamentals and Applications*, 2nd ed.; John Wiley and Sons: New York, 2001.

(30) Ciszkowska, M.; Stojek, Z. Voltammetry in solutions of low ionic strength. Electrochemical and analytical aspects. *J. Electroanal. Chem.* **1999**, *466*, 129.

(31) Beriet, C.; Pletcher, D. A further microelectrode study of the influence of electrolyte concentration on the kinetics of redox couples. *J. Electroanal. Chem.* **1994**, *375*, 213.

(32) Amatore, C.; Paulson, S. C.; White, H. S. Successive electron transfers in low ionic strength solutions. Migrational flux coupling by homogeneous electron-transfer reactions. *J. Electroanal. Chem.* **1997**, *439*, 173.

(33) Ciszkowska, M.; Osteryoung, J. G. Voltammetry of metals at mercury film microelectrodes in the absence and presence of varying concentrations of supporting electrolyte. *Anal. Chem.* **1995**, *67*, 1125.